



# Ultra-massive MIMO for future cell-free heterogeneous networks - **MiFuture**

# Ultra massive MIMO channel models for Mid-band frequencies

# Deliverable 2.1

Grant Agreement Number: 101119643

Project Acronym: MiFuture

Project Title: ultra-massive MIMO for future cell-free heterogeneous networks

Call: HORIZON-MSCA-2022-DN-01

Type of action: HORIZON TMA MSCA Doctoral Networks - Industrial Doctorates

Granting authority: European Research Executive Agency

Project start date: 01/01/2024

VERSION DETAILS	
Original Delivery Date:	27/08/2025
Actual Delivery Date:	27/08/2025
Version:	V1.0
Number Of Pages:	31
Status:	Draft
Dissemination level <sup>1</sup> :	PU

CONTRIBUTIONS		
Participant	Name	
DC4 (UNL)	Omid Abbassi Aghda	
DC6 (ERF / TAU)	Mehmet Ertug Pihtili	
DC11 (KEY)	Joao Ferreira	
DC13 (ULUND)	Aleksandar Birmancevic	

DOCUMENT HISTORY			
Version	Date	Responsible	Description
V0.1	22/08/2025	Aleksandar Birmancevic	First report release

DOCUMENT REVIEWS			
Version Date		Reviewed by	Conclusion <sup>2</sup>
V0.1	26/08/2025	Eduardo Alonso Frech	Document format modifications

 $<sup>^{1}</sup>$ PU = Public, SEN = Sensitive  $^{2}$ e.g. Accepted, Develop, Modify, Re-edit, Update

# Beneficiaries and Partners

## Beneficiaries:

- 1. UNIVERSIDAD CARLOS III DE MADRID (UC3)
- 2. INSTITUTO DE TELECOMUNICAÇÕES (IT)
- 3. TAMPEREEN KORKEAKOULUSAATIO SR (TAU)
- 4. LUNDS UNIVERSITET (ULUND)
- 5. UNIVERSITAT AUTONOMA DE BARCELONA (UAB)
- 6. VODAFONE INTELLIGENT SOLUTIONS ESPANA (VOIS)
- 7. OY L M ERICSSON AB (ERF)
- 8. ERICSSON AB (ERS)
- 9. NOKIA SOLUTIONS AND NETWORKS SP ZOO (NOP)
- 10. NOKIA SOLUTIONS AND NETWORKS OY (NOF)
- 11. ALTYS TECHNOLOGIES (ALT)
- 12. KEYSIGHT TECHNOLOGIES BELGIUM (KEY)

### **Associated Partners:**

- 1. UNIVERSIDADE NOVA DE LISBOA (UNL)
- 2. UNIVERSIDADE DE AVEIRO (UAv)
- 3. UNIVERSIDADE DE COIMBRA (UCo)
- 4. KATHOLIEKE UNIVERSITEIT LEUVEN (KUL)
- 5. KEYSIGHT TECHNOLOGIES UK LIMITED (KEY-UK)

# **Executive Summary**

Considering the vision of MiFuture project that an evolution of ultra-massive MIMO will be a key enabler in the upcoming mobile radio access networks, apparently, nowadays it deserves significant research attention. By addressing the desired goal, its fundamental ingredient, radio channel characterization and modeling, must be carefully considered. Although the mid-band frequencies and particularly Frequency Range 3 represent the (sub)band that is already analyzed in the scope of satellite communications, this time, terrestrial communications are eager for a detailed Frequency Range 3 channel analysis.

Having said that, the report strives to disclose the channel aspects related to both layouts, co-located and distributed ultra-massive MIMO systems. Co-located ultra-massive MIMO operating in an array near field comes with the benefits of channel predictability, reducing its dependence on demanding processing schemes. With the extra-large array aperture, the spatial resolution becomes very high and therefore, the closely separated users may be spatially distinguished. Thus, with the array aperture extensions, non-stationarities over these arrays result in variations of channel statistics. Distributed ultra-massive MIMO reduces the spatial correlations present between antenna elements which could even arise to extensively strong levels in co-located arrays. Depending on a chosen beamforming / receive combining strategy, the spatial correlation comes with advantages and disadvantages. However, distributed systems minimize spatial correlation further opening a door for low computational overhead of these schemes. In that manner, the scheme like Maximum Ratio Combining satisfies performance requirements together with the overhead reduction. Among that, the spatial consistency represents a crucial aspect of experiencing similar scattering environments for close user channels in the angular domain, not only for communication, but also for sensing.

Mid-band channel modeling approaches rely on variations of previously described aspects. The favorable channel model should preferably contain the implementations of as many as possible aspects, and yet, be validated for applications in the frequency range of interest. Hence, the measurement campaigns should have adjustment for indoor and outdoor propagation scenarios with employment of co-located and distributed ultra-massive MIMO arrays. The reports provide insights for different groups that have been dealing with characterization and modeling aspects. From bodies for technical specifications, where 3GPP should be accounted to European Union funded communities, with the COST as a representative, the report discusses different modeling approaches noticing the enhancements made, but also still present limitations. On top of that, attention is given for the overview of efforts IEEE 802.11 makes in order to maintain the bond with achievements of others.

The ongoing activities on redefinition of established frameworks should capture propagation dynamics in existing and novel environments accounting for large antenna apertures. The entire modeling in these conditions may be marked as a challenging one, thus, promising results and conclusions from which the society would highly benefit.

# Contents

1	$\mathbf{Mid}$	l-band	channel models for communication and sensing	1
	1.1	Chann	nels aspects for co-located ultra massive MIMO	1
		1.1.1	Array near field	
		1.1.2	Non-stationarities over the large array	2
		1.1.3	Channel hardening (for small-scale fading)	2
		1.1.4	User orthogonality	2
	1.2	Chann	nels aspects for distributed massive MIMO	2
		1.2.1	Spatial Correlation	2
		1.2.2	Channel Hardening	4
		1.2.3	User Orthogonality	4
	1.3	Chann	nels aspects for sensing	5
		1.3.1	Radar Cross Section	5
		1.3.2	Spatial Consistency	7
2	Mid	l-band	channel modeling approaches	9
	2.1		TR 38.901: Channel Model for Frequencies up to 100 GHz	9
		2.1.1	Key Features of TR 38.901 Channel Model	9
		2.1.2	Modeling Enhancements and Limitations in TR 38.901	10
		2.1.3	3GPP 38.901 channel model for IIoT	10
		2.1.4	Overview of ISAC in 5G	11
	2.2	Free-sp	pace Path Loss RIS-assisted Wireless Communications	14
	2.3	COST	2100/INTERACT	18
		2.3.1	Single-link implementation	18
		2.3.2	Multi-link extension	19
		2.3.3	Massive MIMO extensions	20
		2.3.4	Extension for D-MIMO	20
		2.3.5	Other extensions	21
	2.4	WiFi s	sense and 802.11 distributed MIMO	21
3	Sun	nmary	and conclusions	23

# Chapter 1

# Mid-band channel models for communication and sensing

Fifth-generation (5G) wireless networks are designed to operate in Frequency Range 1 (FR1), spanning 0.4 to 6 GHz, and Frequency Range 2 (FR2), covering 24 to 71 GHz. Future sixth-generation (6G) networks aim to deliver greater bandwidth and higher data rates while addressing the limitations of the current 5G frequency bands. To support the deployment of extremely large multiple-input multiple-output (MIMO) arrays, which require shorter wavelengths compared to those in FR1, and to address the significant coverage limitations in FR2, also known as the millimeter wave (mmWave) band, due to its high susceptibility to blockage in the wireless medium and its sensitivity to the distance between the transmitter and receiver, an evolution toward the mid-band frequency spectrum from 7 to 20 GHz, referred to as Frequency Range 3 (FR3), has attracted increasing attention from both industry and academia [1]. This evolution could enable up to a 20-fold increase in network capacity while largely maintaining the existing site grid in urban areas [2].

This report investigates the potential of promising mid-band frequencies by analyzing their channel modeling characteristics from the perspectives of ray tracing, geometry-based stochastic channel models, stochastic channel models, and spatial consistency. Furthermore, the report discusses their potential applications in both communication and sensing, along with an overview of currently deployed frequency bands.

# 1.1 Channels aspects for co-located ultra massive MIMO

# 1.1.1 Array near field

In ultra massive MIMO systems with co-located arrays, the aperture of the antenna array becomes extremely large, such that many users may fall within the near-field (or Fresnel) region of the array. In this region, the commonly used far-field plane-wave approximation no longer holds, and spherical wavefronts must be considered for accurate modeling. The boundary between near-field and far-field is typically characterized by the Fraunhofer distance, given by

$$d_{\rm F} = \frac{2D^2}{\lambda},\tag{1.1}$$

where D is the largest dimension of the antenna array, and  $\lambda$  is the wavelength. When users are located within  $d_{\rm F}$ , the channel exhibits distance-dependent spatial characteristics, allowing for enhanced focusing and resolution in beamforming designs.

## 1.1.2 Non-stationarities over the large array

Due to the extreme physical size of the antenna array (characterized by a large D), the propagation environment may appear different to different portions of the array. This leads to spatial non-stationarities, where the channel statistics, such as angular spreads, path gains, and delay profiles, vary across the array aperture. Such behavior violates the traditional assumption of wide-sense stationarity along the array and must be explicitly modeled to ensure accurate channel estimation, calibration, and optimal array processing.

# 1.1.3 Channel hardening (for small-scale fading)

Co-located Ultra massive MIMO offers significant channel hardening, where the stochastic fluctuations due to small-scale fading average out as the number of antennas increases. This effect causes the effective channel gain to converge toward a deterministic value, making it more predictable and less sensitive to instantaneous variations. In co-located configurations, where antennas are tightly grouped and share a common propagation environment, this averaging effect is particularly pronounced. As a result, signal processing tasks such as power control, beamforming, and modulation adaptation become more stable and less dependent on real-time channel feedback. Furthermore, the reduced channel variability diminishes the need for frequent and complex channel estimation, lowering overhead and improving system efficiency—especially critical for latency-sensitive applications.

# 1.1.4 User orthogonality

The large number of spatial degrees of freedom in ultra massive MIMO allows for a high level of user orthogonality, especially in co-located configurations where all antennas share a common phase reference and synchronization. The extensive array aperture provides ultra-fine angular resolution, making it possible to spatially distinguish users even when their angles of arrival or departure are very close. In the near-field regime, this separation is further enhanced by the availability of distance-dependent channel signatures, which introduce an additional spatial dimension for discrimination. This improved spatial separability significantly enhances multi-user multiplexing capability, reduces inter-user interference, and supports dense user deployments with minimal degradation in performance. Furthermore, near-orthogonal channels reduce the need for complex scheduling and coordination, leading to higher spectral efficiency and more robust system scalability.

# 1.2 Channels aspects for distributed massive MIMO

# 1.2.1 Spatial Correlation

Massive multiple-input multiple-output systems are a promising solution for achieving high spectral efficiency in future wireless networks. These systems utilize a large number of antennas at base stations to serve multiple users simultaneously through spatial multiplexing. However, when antennas are co-located in centralized configurations, spatial correlation among antenna elements can arise, which degrades the orthogonality of user channels and reduces system performance. Distributed antenna systems mitigate this issue by spatially separating antenna clusters across the cell area, thereby reducing correlation and enhancing coverage diversity [3].

When a fixed number of antennas are positioned either closely or further apart, the spacing affects the overall design. The primary motivation for reducing the distance between antenna elements is to accommodate a larger number of antennas within a limited physical area, which is essential for developing compact large-scale MIMO transceivers [4]. Although many studies assume that wireless channels are uncorrelated, spatial correlation occurs in practice and must be thoroughly examined when designing a massive MIMO system.

As with any M-dimensional vector, the channel  $\mathbf{h}_{ik}^l \in C^M$  is defined by its norm  $\|\mathbf{h}_{ik}^l\|$  and its direction  $\frac{\mathbf{h}_{ik}^l}{\|\mathbf{h}_{ik}^l\|}$  within the vector space. In fading channels, both components are treated as random variables. Under the uncorrelated Rayleigh fading model described in [5], the squared norm  $\|\mathbf{h}_{ik}^l\|^2$  follows a scaled chi-squared distribution and is statistically independent of the direction  $\frac{\mathbf{h}_{ik}^l}{\|\mathbf{h}_{ik}^l\|}$ , which is uniformly distributed over the unit sphere in  $C^M$ . This behavior defines a spatially uncorrelated channel.

unit sphere in  $C^M$ . This behavior defines a spatially uncorrelated channel.

A fading channel  $h \in C^M$  is considered spatially uncorrelated if the channel gain  $\|h\|^2$  and the channel direction  $\frac{h}{\|h\|}$  are independent random variables, with the direction uniformly distributed over the unit sphere. If these conditions are not met, the channel is deemed spatially correlated. This definition highlights the stringent requirements for a channel to be spatially uncorrelated, which explains why real-world channels are typically spatially correlated to varying degrees. Several physical factors contribute to this correlation: the propagation environment tends to generate more multipath components from certain spatial directions than others; base station antennas exhibit spatially varying radiation patterns and polarization characteristics; and the geometry of the antenna array can lead to spatial undersampling or oversampling. Together, these aspects result in practical channels exhibiting spatial correlation [5].

In [3], the impact of spatial correlation on uplink performance in distributed massive MIMO systems is analyzed using a deterministic channel model. The channel covariance matrices  $R_{bcu}$  encapsulate path-loss, shadowing, and spatial correlation effects. A uniform circular array is used to model the antenna geometry, and the power azimuth spectrum is represented by a truncated Laplacian distribution. This modeling approach allows each user to experience a distinct spatial correlation matrix, reflecting realistic propagation conditions.

Two linear beamforming strategies are considered: maximal ratio combining (MRC) and minimum mean squared error (MMSE). MRC is computationally simple but suboptimal in the presence of interference, while MMSE offers superior interference suppression at the cost of increased complexity. Simulation results show that spatial correlation slightly degrades the performance of MRC yet enhances the performance of MMSE. This is because MMSE can exploit the structure of spatial correlation to suppress interference more effectively, whereas MRC lacks such capability.

The deterministic equivalent signal-to-interference-plus-noise ratio for maximal ratio combining is given by

$$\bar{\eta}_{bu} = \frac{(\operatorname{tr} \Phi_{bbu})^2}{\sigma_b^2 p_r \operatorname{tr} \Phi_{bbu} + \sum_{(c,v) \neq (b,u)} \operatorname{tr} R_{bcv} \Phi_{bbu} + \sum_{c=b} (\operatorname{tr} \Phi_{bcu})^2}$$
(1.2)

where  $\Phi_{bbu}$  is the covariance of the MMSE channel estimate,  $R_{bcv}$  is the channel covariance matrix from user v in cell c to base station b, and  $\sigma_b^2$  is the noise variance.

Moreover, [3] compares centralized and distributed antenna configurations, including one-cluster, three-cluster, and eight-cluster layouts. Increasing the number of antenna clusters improves the uplink sum-rate, particularly under MMSE beamforming. Distributed configurations reduce spatial correlation and increase channel diversity, leading to improved system performance. Furthermore, user grouping and remote radio head (RRH) selection strategies are proposed to optimize MRC performance in distributed antenna systems. By assigning each user to its preferred remote radio head based on signal-to-interference-plus-noise ratio metrics, the system can achieve performance close to that of minimum mean squared error with significantly lower complexity.

On top of that, [6] showed that spatial correlation can be beneficial for MMSE receivers due to enhanced interference suppression capabilities. [7] emphasized the importance of accurate channel modeling and note that spatial correlation must be considered in realistic deployments. [8] demonstrated that user channels become decorrelated as the number of antennas increases, and that distributed antennas accelerate this effect by introducing spatial diversity.

In conclusion, spatial correlation plays a nuanced role in distributed massive MIMO systems. While it can hinder performance under simple beamforming schemes, it can be leveraged under advanced strategies to improve interference management. Distributed antenna architectures, combined with intelligent user grouping and remote radio head selection, offer a promising approach to mitigate correlation effects and enhance uplink performance in massive MIMO networks

# 1.2.2 Channel Hardening

A single-cell Massive MIMO system is considered, consisting of an M-antenna base station (BS) and K single-antenna users, where M > K. The channel between the BS and the kth user is represented by an  $M \times 1$  channel vector, denoted by  $\mathbf{g}_k$ , and is modeled as [9]:

$$\mathbf{g}_k = \sqrt{\beta_k} \mathbf{h}_k,\tag{1.3}$$

where  $\beta_k$  represents large-scale fading, which is assumed to remain constant over many coherence intervals, and  $\mathbf{h}_k$  is an  $M \times 1$  small-scale fading channel vector. The elements of  $\mathbf{h}_k$  are assumed to be uncorrelated, zero-mean, and unit-variance random variables (RVs), which are not necessarily Gaussian distributed. Furthermore,  $\mathbf{h}_k$  and  $\mathbf{h}_{k'}$  are assumed to be independent for  $k \neq k'$ . The mth elements of  $\mathbf{g}_k$  and  $\mathbf{h}_k$  are denoted by  $g_k^m$  and  $h_k^m$ , respectively. Furthermore,  $\mathbf{h}_k$  and  $\mathbf{h}_{k'}$  are assumed to be independent for  $k \neq k'$ . The mth elements of  $\mathbf{g}_k$  and  $\mathbf{h}_k$  are denoted by  $g_k^m$  and  $h_k^m$ , respectively.

Channel hardening is a phenomenon where the norms of the channel vectors  $\{\mathbf{g}_k\}$ , for  $k = 1, \dots, K$ , fluctuate only slightly. We say that the propagation offers channel hardening if

$$\frac{\|\mathbf{g}_k\|^2}{E\{\|\mathbf{g}_k\|^2\}} \xrightarrow{P} 1, \quad \text{as } M \to \infty, \quad k = 1, \dots, K.$$

$$\tag{1.4}$$

Channel hardening refers to the phenomenon where beamforming transforms a fading multi-antenna channel into an almost deterministic scalar channel. This provides several advantages, as the network operation becomes less dependent on small-scale channel variations [10]. When the channel exhibits hardening, the sum capacity becomes independent of small-scale fading, allowing system-level operations such as scheduling, power allocation, and interference management to be performed based on the large-scale fading time scale rather than the small-scale fading time scale. This significantly reduces the overhead associated with these system functions [9]. Furthermore, channel hardening eliminates the need for instantaneous channel state information (CSI) at the receiver for signal detection. Instead, the receiver requires only statistical knowledge of the channel gains, which reduces the resources needed for channel estimation, including power consumption and training duration [9].

## 1.2.3 User Orthogonality

The channel vector from the M antennas to user k is denoted by

$$\mathbf{g}_k = [g_{1,k}, \dots, g_{M,k}]^T,$$
 (1.5)

where each element is given by

$$g_{m,k} = \sqrt{l(d_{m,k})} h_{m,k}.$$
 (1.6)

Favorable propagation refers to the scenario in which users' channel vectors are nearly orthogonal, enabling efficient spatial separation. Mathematically, this condition is expressed as

$$\mathbf{g}_k^H \mathbf{g}_j = \begin{cases} 0 & \text{if } k \neq j, \\ \|\mathbf{g}_k\|^2 \neq 0 & \text{if } k = j. \end{cases}$$
 (1.7)

When this orthogonality condition holds, each user experiences communication performance comparable to operating alone in the network. Although perfect orthogonality is rarely achieved in practice, it can be approximated as the number of antennas grows large, leading to what is known as asymptotically favorable propagation [10].

The probability that two users at random locations experience favorable propagation conditions is quantified by the metric

$$p_{\gamma} = P[X_{fp} \le \gamma]. \tag{1.8}$$

This probability is computed over various network realizations, each yielding different distance vectors  $\mathbf{d}_k$  and  $\mathbf{d}_j$ . Under asymptotically favorable propagation, as the antenna density increases,  $p_{\gamma}$  is expected to converge to one for any threshold  $\gamma \geq 0$ . From a practical standpoint, it is desirable that  $p_{\gamma}$  remains high even for small values of  $\gamma$ , indicating robust favorable propagation across typical network deployments. Favorable propagation means that the users' channel vectors are almost orthogonal, which facilitates efficient multi-user communication [10].

# 1.3 Channels aspects for sensing

Perceptive networks in 6G systems will play a vital role by integrating sensing functionalities into future wireless networks. This section discusses two key concepts, namely radar cross section (RCS) and spatial consistency, within the integrated sensing and communication (ISAC) paradigm, primarily from the perspective of ISAC channel modeling as defined by the Third Generation Partnership Project (3GPP) [11].

#### 1.3.1 Radar Cross Section

RCS, denoted as  $\sigma$ , is a parameter used to characterize the reflective properties of an object when illuminated by radar waves, which indicates the object's ability to reflect electromagnetic waves. It indicates the target's ability to reflect radar energy. Specifically:

- RCS is a scalar value measured in square meters (m<sup>2</sup>).
- It represents the intensity of the backscattered energy received at the radar's receiving antenna.
- A target with a larger RCS produces a stronger echo, making it more easily detectable by the radar system.

The reflecting properties of a point-scatterer sensing object determine the power of the backscattered signal received at the sensing receiver. The radar range equation (RRE) is a deterministic model that relates received echo power to transmitted power in terms of various system design parameters. It is a fundamental relation used for basic system design and analysis. Assume an isotropic radiating element transmits a waveform of power  $P_t$  watts into a lossless medium. The isotropic transmitted power density at range R with directive antennas is:

$$Q_t = \frac{P_t G}{4\pi R^2} \quad (W/m^2) \tag{1.9}$$

If the target has an RCS  $\sigma$ , the backscattered power is

$$P_b = \frac{P_t G \sigma}{4\pi R^2} \tag{1.10}$$

The backscattered power density at the radar is:

$$Q_b = \frac{P_t G \sigma}{(4\pi)^2 R^4} \quad (W/m^2)$$
 (1.11)

The received power using effective aperture  $A_e = \frac{\lambda^2 G}{4\pi}$  is:

$$P_r = A_e Q_b = \frac{P_t G A_e \sigma}{(4\pi)^2 R^4} = \frac{P_t G^2 \lambda^2 \sigma}{(4\pi)^3 R^4}$$
(1.12)

Including system and atmospheric losses  $L_s$  and  $L_a(R)$  [12]::

$$P_r = \frac{P_t G^2 \lambda^2 \sigma}{(4\pi)^3 R^4 L_s L_a(R)}$$
 (1.13)

The received signal expression in (1.13) is a function of the RCS of a point-scatterer sensing target. Several factors influence the RCS of the sensing target and consequently affect the received power  $P_r$ . These factors are explained in detail below, following the modeling approach in [11].

The shape of an object influences the physical processes of reflection, diffraction, and scattering of electromagnetic waves from its surface, which in turn affects both the magnitude and distribution of the RCS. In general, for a given size, objects with smooth curves and surfaces tend to have a smaller RCS, as these shapes cause the incident signal to be more evenly dispersed, reducing strong reflections and scattering. Conversely, objects with sharp edges and angles typically have a larger RCS due to increased scattering and reflective surfaces.

Frequency has a significant impact on the RCS of a target. In general, the RCS increases with increasing frequency. At low frequencies, the RCS is typically larger because the longer wavelengths of electromagnetic waves can envelop and interact with large-sized targets more effectively. At higher frequencies, however, the RCS is usually smaller since the shorter wavelengths can pass by small-sized targets more easily, resulting in reduced reflectivity. Moreover, the change in RCS across different frequencies is not uniform.

The orientation of an object also plays a key role in RCS behavior. It is assumed that the polarization of the target is linked to the orientation of the object and should be decoupled from the RCS modeling in order to analyze these effects independently.

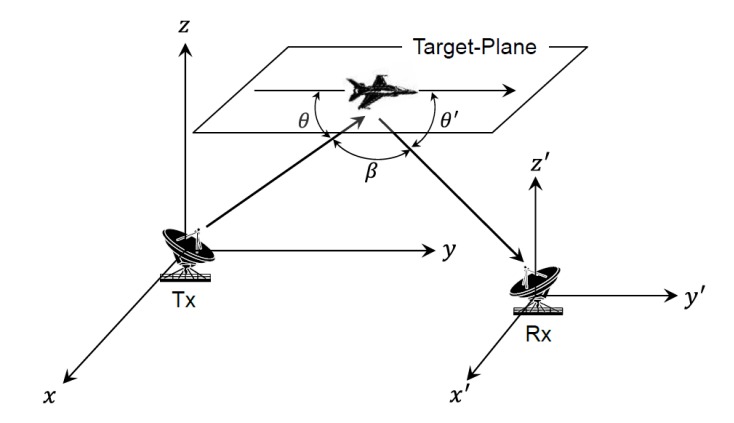


Figure 1.1: Incident angle, the scatter angle, and the bistatic angle of a sensing target.

To accurately assess the impact of incident and scatter angles, it is necessary to define each angle associated with the bistatic configuration. As illustrated in Figure 1.1, consider a target (e.g., an aircraft) located in the target plane, which is parallel to the x-y plane. For simplicity and without considering antenna orientation, let the incident angle from the transmitter to the target be denoted by  $\theta$ , and the scatter angle toward the receiver by  $\theta'$ . The bistatic angle  $\beta$  can then be geometrically derived as a function of these two angles, i.e.,  $\beta = f(\theta, \theta')$ . The aspect dependence of the RCS arises from its variation with both the incident angle  $\theta$  and the scatter angle  $\theta'$ . It should be noted that when the antenna orientation is taken into account, the angles  $\theta$  and  $\theta'$  are no longer referred to simply as the incident and scatter angles. Instead, they must be derived from the aspect angle and the respective orientations of the transmit and receive antennas.

## 1.3.2 Spatial Consistency

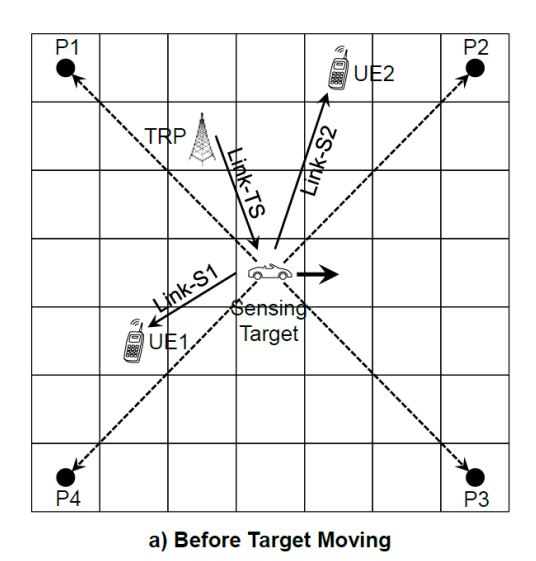
The RCS of an object is generally not subject to temporal variation, as it is typically an inherent property of the object that does not change over time. In radar systems, the RCS of a specific target is often treated as a static value. However, in space, the RCS of an object varies with the observation angle and the relative position between the radar and the target. This implies that an object exhibits different reflective properties to radar waves depending on the direction and location of observation. Therefore, it is important to consider spatial consistency when modeling the RCS of an object. For example, analyzing the RCS at different orientations and angles can help the receiver detect and track the target more effectively [11].

Channel consistency refers to the phenomenon where two closely located channels in spatial or temporal domains may experience similar scattering environments. In ISAC scenarios, exploiting information from a previous time snapshot or a neighboring location requires both temporal and spatial consistency. These forms of consistency are crucial for enhancing sensing accuracy and communication reliability in dynamic environments [13].

Spatial consistency is a key concept relevant to both communication and sensing. It can be classified according to whether it applies to single-target-related sensing channels or multi-target-related sensing channels. While TR38.901 defines spatial consistency for communication channels, the same mechanism cannot be directly applied to sensing channels, and therefore enhancements are necessary. The following discusses how spatial consistency can be realized for sensing, based on the approach in [11].

## Spatial Consistency for Single-Target-Related Sensing Channels

For the ISAC channel based on a stochastic approach, to model spatial consistency in single-target-related channels for bistatic and monostatic sensing mode, The channel parameter set is classified into the network level (i.e., all-correlated) and the sensing-target-specific level. For network-level correlations, the corresponding parameter set remains the same as defined in TR38.901. For sensing-target-specific level correlations, on the other hand, the spatial consistency is preserved within the parameter sets of the channel links from sensing transmitters and sensing receivers to the same sensing target, as shown in Figure 1.2.



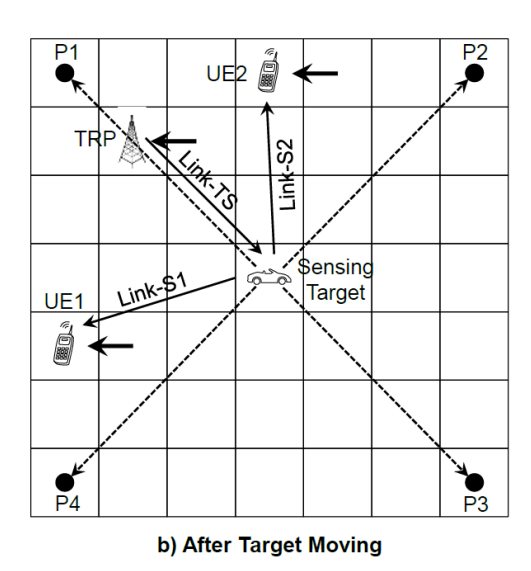


Figure 1.2: Spatial consistency procedure for bi-static sensing node before and after target moving.

For a mono-static sensing model, the sensing transmitter and sensing receiver are deployed at the same position, which can be considered as a special case of the bistatic sensing-target-specific model. Considering that the sensing transmitter and receiver are regarded as one node for monostatic, the spatial consistency

modeling can ideally follow what is defined in TR38.901 and 3GPP TR38.900 for TRP monostatic. All the parameters and the corresponding correlation types are listed in Table 1.1.

Parameters	TR38.901	Sensing channel
Delays	Site-specific level	Sensing-target-specific level
Cluster powers	Site-specific level	Sensing-target-specific level
AOA/ZOA/AOD/ZOD offset	Site-specific level	Sensing-target-specific level
AOA/ZOA/AOD/ZOD sign	Site-specific level	Sensing-target-specific level
Random coupling	Site-specific level	Sensing-target-specific level
XPR	Site-specific level	Sensing-target-specific level
Initial random phase	Site-specific level	Sensing-target-specific level
LOS/NLOS states	Site-specific level	Sensing-target-specific level
Blockage (Model A)	All-correlated	All-correlated
O2I penetration loss	All-correlated	All-correlated
Indoor distance	All-correlated	All-correlated
Indoor states	All-correlated	All-correlated

Table 1.1: Correlation type of channel parameter set

# Spatial Consistency for Multi-Targets-Related Sensing Channels

The previously proposed method considers only the spatial consistency of links associated with a single target, which does not ensure spatial consistency across different targets. As illustrated in Figure 1.3, when three targets and user equipments (UEs) are spatially distributed, the links TRP-Target1-UE1, TRP-Target2-UE2, and TRP-Target3-UE3 should be treated as spatially correlated. To model spatial con-

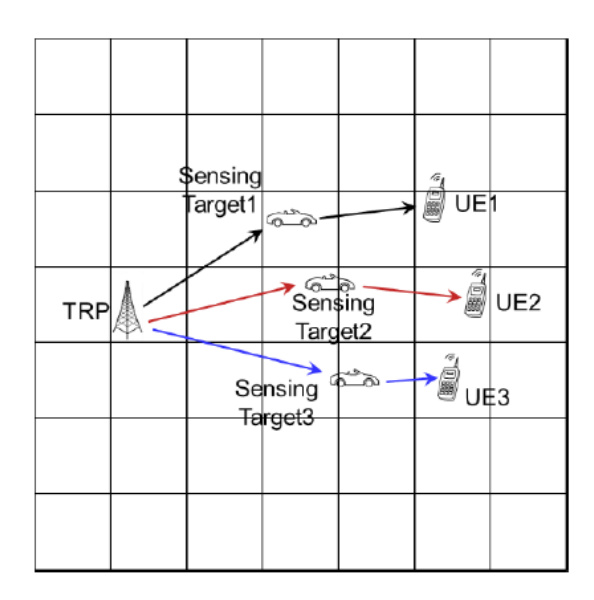


Figure 1.3: Different links through different targets.

sistency for the links across different targets, the method called the random variable interpolation method based on correlated grid topologies, abbreviated as RVIM, is employed. In this method, the correlation of grids associated with different targets is first modeled, and then interpolation techniques are applied to establish spatial consistency between the different targets [11].

# Chapter 2

# Mid-band channel modeling approaches

# 2.1 3GPP TR 38.901: Channel Model for Frequencies up to 100 GHz

The 3rd generation partnership project (3GPP) Technical Report TR 38.901, published as European telecommunications standards institute (ETSI) TR 138 901 V18.0.0, defines a comprehensive and standardized radio channel model for frequencies ranging from 0.5 GHz to 100 GHz, with a particular emphasis on millimeter wave (mmWave) bands above 6 GHz. This work was initiated following the approval of the Study Item on "Channel Model for Frequency Spectrum Above 6 GHz" at the technical specification group (TSG) radio access network (RAN) meeting #69. The goal of this study was to assess existing knowledge and develop accurate models for high-frequency wireless propagation, including aspects such as spectrum allocation, deployment scenarios, and measurement data [14].

The resulting channel model is designed to support both link-level and system-level simulations for new radio (NR) and future wireless systems. It aligns closely with earlier models used for sub-6 GHz frequencies, such as [14]

- The 3D spatial channel model (SCM) defined in 3GPP TR 36.873, which introduced three-dimensional modeling of signal propagation, including elevation angles, to better represent urban and indoor environments [15].
- The international mobile telecommunications (IMT)-Advanced channel models specified in ITU radiocommunication sector (ITU-R) M.2135 by the international telecommunication union (ITU), which were used to evaluate 4G technologies.

Further enhancements were introduced at TSG RAN meeting #81, where a new Study Item on Channel Modeling for Indoor Industrial Scenarios was approved. This led to the development of specialized models for indoor factory environments, based on new measurement campaigns and literature reviews. These additions are also documented in TR 38.901 [14].

#### 2.1.1 Key Features of TR 38.901 Channel Model

Key features of the TR 38.901 channel model include [14]

- Support for multiple deployment scenarios: urban microcell (UMi) (street canyon), urban macrocell (UMa), rural macrocell (RMa), indoor office, and indoor factory.
- Bandwidth support: up to 10% of the center frequency, with a maximum of 2 GHz.
- Mobility support: for one or both ends of the communication link.

- Spatial consistency: achieved through correlation of large-scale parameters (LSPs) and small-scale parameters (SSPs), as well as line-of-sight (LOS) and non-line-of-sight (NLOS) conditions.
- Large antenna array support: based on the far-field assumption, where the channel is considered stationary over the size of the array, meaning that the channel characteristics (e.g., fading, angles of arrival) do not vary significantly across the physical extent of the antenna array.

While 3GPP TR 38.901 provides channel models spanning a wide frequency range from 0.5 GHz to 100 GHz, this summary focuses specifically on the mid-band spectrum, including both the traditional mid-band (typically defined as 1–6 GHz) and the emerging new mid-band (6–24 GHz). Mid-band frequencies are of particular importance in 5G deployments due to their balance between coverage and capacity. Unlike low-band frequencies, which offer wide coverage but limited bandwidth, and high-band (mmWave) frequencies, which provide high capacity but limited range, mid-band offers a compelling trade-off. In particular, it is highly desirable to utilize the mid-band efficiently for its benefits of broad coverage, low cost, and massive access support [16]. Meanwhile, the new mid-band is gaining attention for its potential to deliver wider bandwidths with better propagation characteristics than mmWave, making it a strong candidate for future 6G systems

# 2.1.2 Modeling Enhancements and Limitations in TR 38.901

In addition to its broad frequency and deployment support, TR 38.901 introduces several modeling enhancements that extend the earlier 3GPP 3D channel model. These include frequency-dependent modeling of parameters such as delay spread, angular spread, and cluster power, as well as oxygen absorption effects in the 53–67 GHz range. The model achieves higher temporal and spatial resolution for large bandwidths and massive multiple-input multiple-output (MIMO) (mMIMO) by allowing unequal intra-cluster delays and powers, and by randomly generating offset angles for rays within a cluster. It also incorporates a hybrid map-based approach that combines stochastic and deterministic components, enabling more realistic modeling in complex environments. Ground reflections are modeled separately from LoS and NLoS components to capture significant fading effects observed in mmWave measurements.

Despite these advancements, the model has limitations, including restricted support for dual mobility, antenna array non-stationarity, and spherical wave propagation. Moreover, only four scenarios: UMi, UMa, RMa, and indoor office are evaluated.

## 2.1.3 3GPP 38.901 channel model for IIoT

Industrial Internet of Things (IIoT) is a key Fifth Generation (5G) use case, particularly for Ultra-Reliable and Low-Latency Communications (URLLC) and Massive Machine-Type Communications (mMTC), where reliable and low-latency communication is essential. Traditional indoor channel models do not capture the complex propagation conditions in industrial environments, which include dense machinery, metallic surfaces, and electromagnetic interference. To address this, 3GPP extended TR 38.901 to include indoor industrial scenarios, enabling more accurate modeling for IIoT applications such as Automated Guided Vehicle (AGV)s and remote-controlled machinery. This extension is crucial for designing robust wireless systems in smart factories and similar settings.

A representative IIoT scenario is illustrated in Fig. 2.1, where technologies such as Multi-access Edge Computing (MEC), device-to-device (D2D) communication, beamforming, and mmWave are integrated to support ultra-dense connectivity among devices like AGVs, mechanical arms, and control centers in a smart factory environment.

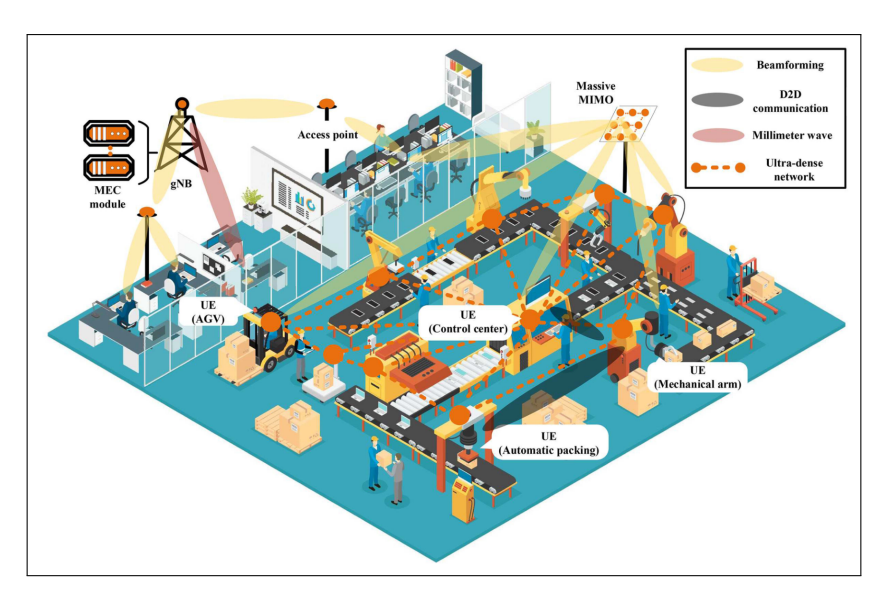


Figure 2.1: One possible IIoT scenario in a smart factory, illustrating technologies such as MEC, D2D communication, beamforming, and mmWave, supporting ultra-dense connectivity among devices like AGVs, mechanical arms, and control centers [17].

## Characteristics of InF Scenarios for Channel Modeling

The propagation environment plays a critical role in wireless channel modeling, making it essential to accurately describe the target scenario. Unlike the indoor office scenario defined in 3GPP TR 38.901, industrial factory (InF) environments, such as warehouses, manufacturing plants, and assembly rooms, exhibit distinct characteristics: larger physical dimensions, higher ceilings (5–25 m), and the presence of large metallic machinery that causes specular reflections and irregular blockage patterns. These differences necessitate a more detailed and flexible modeling approach.

To address this, the InF layout is divided into functional areas (e.g., production, storage, office), and its size is defined by area rather than fixed dimensions, ranging from 20 to 160,000 m<sup>2</sup>. Figures 2.2 and 2.3 compare the indoor office and InF layouts, highlighting the increased area and complexity of the latter. The variability in machine height (0–10 m) complicates the definition of user terminal (UT) height, leading to the use of "clutter-embedded" and "clutter-elevated" antenna height models. Both base station (BS) and UT antennas may be placed above the average machine height to ensure better coverage.

Clutter density defined by the ratio of clutter-occupied area is also considered, with 40% used as the threshold between sparse and dense environments. Based on clutter density and BS antenna height, the NLOS cases are classified into four subscenarios: sparse clutter with low BS (SL), dense clutter with low BS (DL), sparse clutter with high BS (SH), and dense clutter with high BS (DH), as illustrated in Fig. 2.4a and Fig. 2.4b. These refinements enable more accurate simulation and evaluation of wireless systems in HoT scenarios.

### 2.1.4 Overview of ISAC in 5G

5G wireless sensing introduces a novel capability within cellular networks: the ability to perceive the environment using radio signals. By analyzing the transmission, reflection, and scattering of these signals, the system can estimate object distance, angle, and velocity. This dual-purpose functionality, communication and sensing forms the foundation of integrated sensing and communication (ISAC).

The use cases for ISAC are defined in 3GPP TR 22.837 and span a wide range of verticals, including smart homes, transportation, public safety, and industrial automation. According to 3GPP TS 22.137 [18, 19],

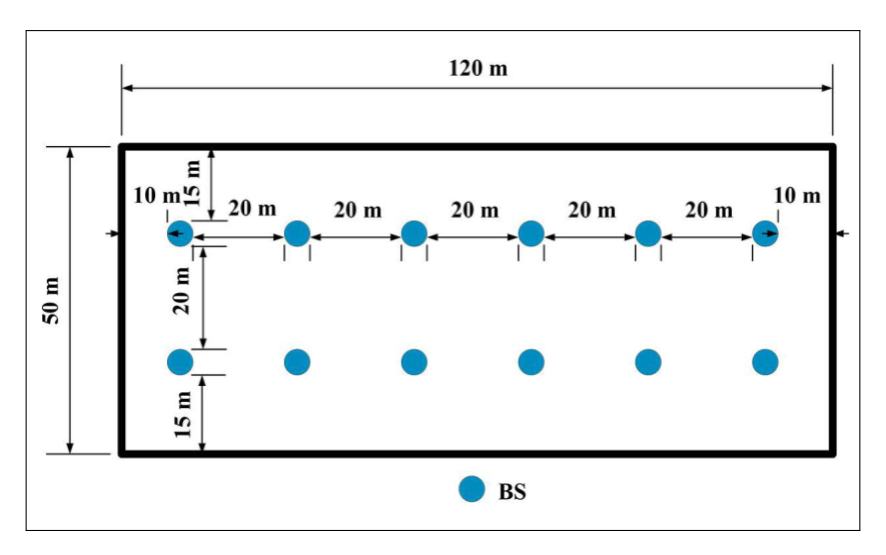


Figure 2.2: Indoor office layout [17].

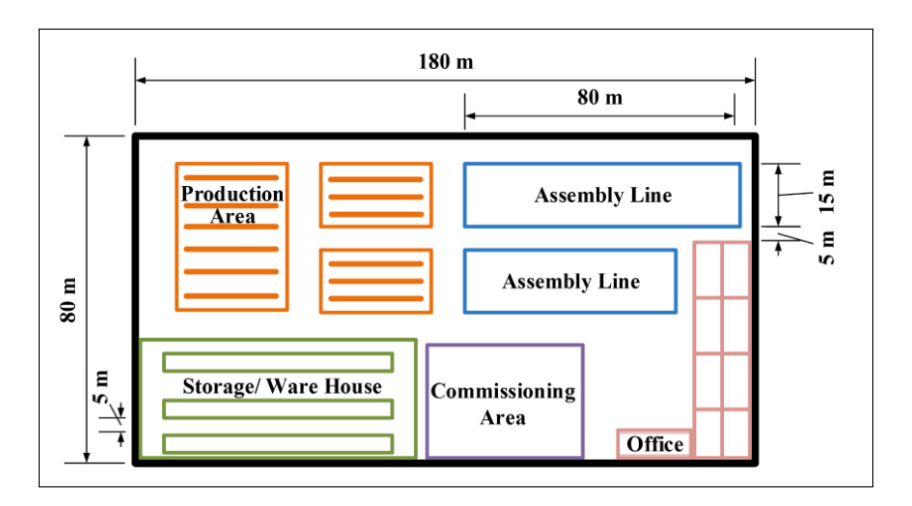


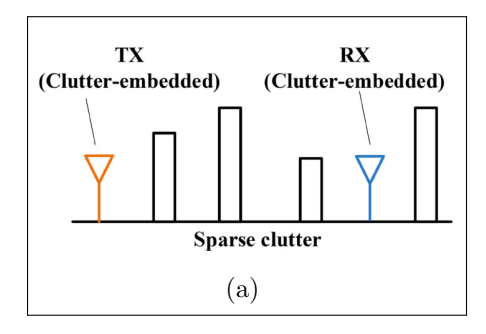
Figure 2.3: IIoT office layout [17].

these use cases are categorized into three classes based on their sensing performance requirements:

- Object detection and tracking
- Environment monitoring
- Motion monitoring

Examples of applications include:

- Intruder detection in smart homes, highways, railways, and factories
- $\bullet$  Collision avoidance and trajectory tracking for UAVs, vehicles, and AGVs
- Automotive maneuvering and navigation
- Public safety operations such as search and rescue
- Environmental monitoring, including rainfall and flooding



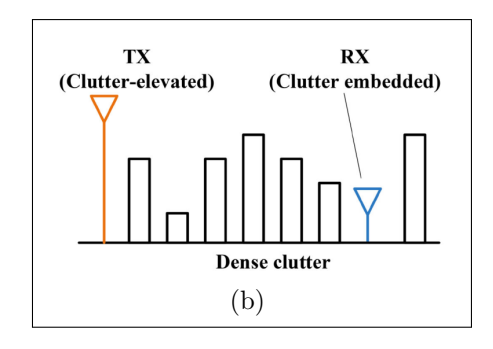


Figure 2.4: a) Sparse clutter, low BS (SL) (b) Dense clutter, high BS (DH) [17].

## • Health and sports monitoring

While this document focuses on one representative use case, readers interested in the full set of 31 use cases can refer to 3GPP TS 22.137 for a comprehensive overview [19].

Although the emphasis is on 5G NR-based sensing, some use cases also incorporate non-3GPP sensors such as radar and cameras. However, the deployment of such services raises concerns around data privacy, regulatory compliance, and user consent. Addressing these challenges is essential for the successful integration of sensing capabilities into 3GPP specifications.

To give an example of one of the use cases defined in 3GPP TR 22.837, we present the scenario of AGV Detection and Tracking in Factories in the following section. This use case illustrates how 5G-based ISAC can enhance safety and operational efficiency in industrial environments by enabling real-time detection of automated guided vehicles and human workers.

# Use Case: AGV Detection and Tracking in Factories in [19]

## Description

In smart manufacturing environments, Automated Guided Vehicles (AGVs) are widely used to transport materials. However, their interaction with human workers introduces safety risks. To mitigate these, 5G-based sensing systems can be deployed to detect and track AGVs and workers in real time.

The 5G system utilizes RAN entities and UEs to transmit and receive sensing reference signals. These signals are processed to generate 3GPP sensing data, which is then analyzed to detect the presence and proximity of AGVs and humans. This is particularly useful for legacy AGVs that lack onboard sensing capabilities.

# **Pre-conditions**

A factory operated by Company #A deploys a 5G-based sensing system. AGVs follow predefined routes, while workers are distributed across the factory floor. The sensing infrastructure includes RAN nodes and UEs configured to monitor specific areas and report sensing data to a central processing entity, either on-premises or in the cloud.

#### Service Flow

The service flow for AGV detection and tracking in a 5G-enabled factory is illustrated in Figure 2.5. The sensing system uses 3GPP sensing data collected from RAN entities and UEs to monitor AGV movement and worker proximity.

1. A worker named Alex is performing maintenance near a conveyor belt.

- 2. AGV#1 approaches Alex's location with a heavy load.
- 3. The sensing system detects the proximity of AGV#1 to Alex using data from RAN nodes and Alex's UE. A warning is issued to Alex.
- 4. AGV#2 enters a high-risk area with dense equipment and personnel. The system detects its presence and alerts nearby workers, including John and Emma.
- 5. In another scenario, John—who does not carry a UE—is tracked using RAN-based sensing. A warning is triggered when he comes close to an AGV.

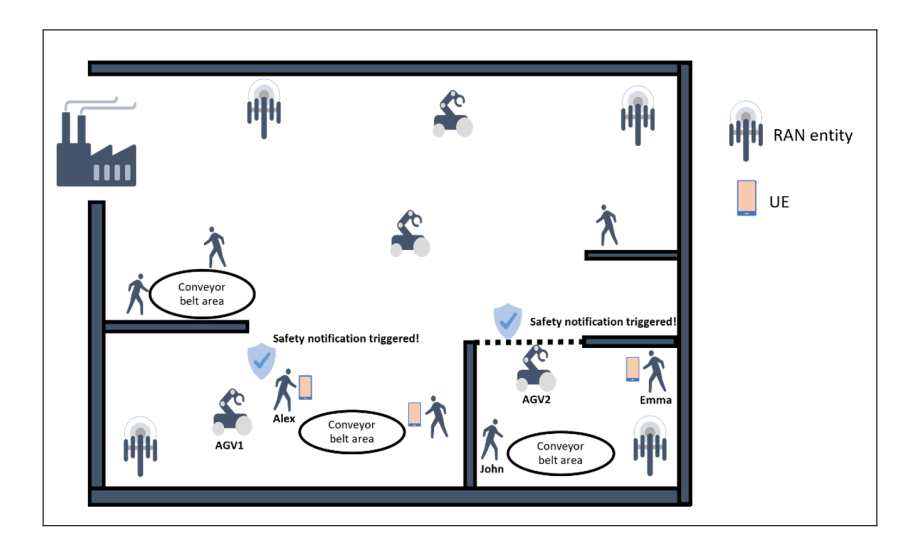


Figure 2.5: AGV presence and proximity detection [19].

## Post-conditions

The system successfully prevents potential collisions, enhancing worker safety and operational efficiency. This demonstrates the value of 5G-based ISAC in industrial automation.

# 2.2 Free-space Path Loss RIS-assisted Wireless Communications

This section presents a channel modeling framework adopted for Reconfigurable Intelligent Surface (RIS)-assisted wireless communication systems [20]. The primary focus is on the analysis of a free-space path loss model within non-line-of-sight (N-LoS) deployment scenarios, aiming to enhance coverage in millimeter-wave (mmWave) systems. We consider a general single-input single-output (SISO) configuration where the RIS operates as a passive planar array between the transmitter and the receiver, illustrated in Fig.2.6. Given the aim of isolating and understanding the RIS-induced propagation characteristics, we deliberately exclude the direct line-of-sight path between the transmitter and receiver from the model. Here, a rectangular RIS is composed of N rows and M columns of unit cells, each denoted by  $U_{n,m}$ . These cells have dimensions  $d_x$  and  $d_y$ , corresponding to their width and length. The distances from the transmitter and receiver to a specific unit cell  $U_{n,m}$  are represented by  $r_{n,m}^t$  and  $r_{n,m}^r$ , respectively. Each unit cell has an associated reflection coefficient  $\Gamma_{n,m}$ , and its normalized power radiation pattern is described by  $F(\theta,\varphi)$ . The scattering gain of an individual cell is given by G. The angular relationships are captured by various elevation and azimuth angles. From the center of the RIS to the transmitter and receiver, the angles are denoted  $(\theta_t, \varphi_t)$  and  $(\theta_r, \varphi_r)$ , respectively. From the unit cell  $U_{n,m}$  to the transmitter and receiver, the angles are denoted  $\theta_t$ ,  $\theta_t$ 

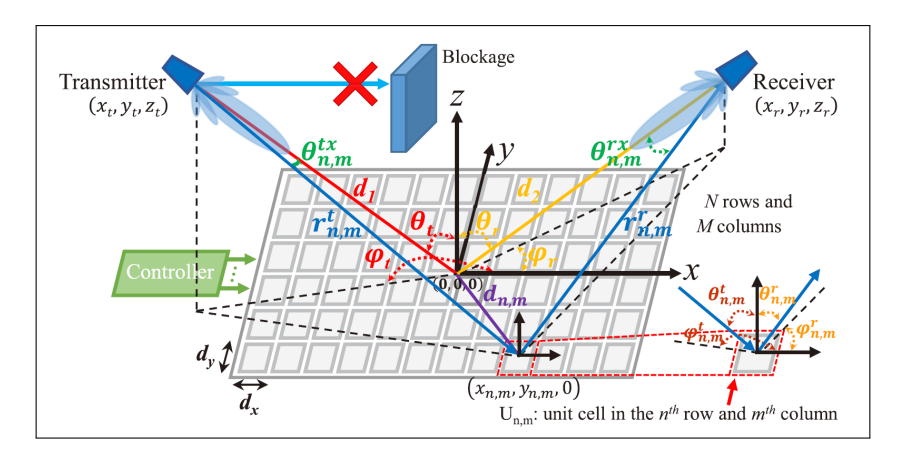


Figure 2.6: The considered RIS-assisted wireless communication system. [20]

and  $(\theta_{n,m}^r, \varphi_{n,m}^r)$ . Similarly, the angles from the transmit and receive antennas to the unit cell  $U_{n,m}$  are given by  $(\theta_{n,m}^{tx}, \varphi_{n,m}^{tx})$  and  $(\theta_{n,m}^{rx}, \varphi_{n,m}^{rx})$ , respectively. The transmit and receive antennas are characterized by their respective gains,  $G_t$  and  $G_r$ , and their normalized power radiation patterns,  $F^{tx}(\theta, \varphi)$  and  $F^{rx}(\theta, \varphi)$ . The system operates at a wavelength  $\lambda$ , and the transmitted signal has power  $P_t$ .

The channel expression shows how the power of the received signal varies with different system parameters. Specifically, it is shown to depend on several key elements: the power we transmit, the antenna gains at both ends, the gains and sizes of the unit cells, the square of the carrier wavelength, and the distances between the RIS and the communicating nodes. Additionally, how the antennas' radiation patterns interact with the RIS unit cells, along with the phase and amplitude of the reflection coefficients, is also important. However, because these factors are interconnected, their exact effects on path loss can be complex and need more study. This model also highlights the reciprocity property of RIS-assisted connections, meaning that the received power stays the same if we swap the transmitter and receiver. This feature is especially useful for time division duplex (TDD) systems, as it helps with channel reciprocity in uplink and downlink beamforming design.

To enable a generalizable analysis across diverse deployment contexts, we consider three representative propagation scenarios involving reconfigurable intelligent surfaces (RIS): far-field beamsteering for single-user enhancement, near-field beamfocusing for single-user enhancement, and controlled plane-wave illumination in compact antenna test range (CATR) environments. In the case of CATR, only the propagation from the RIS to the receiving probe is considered, as the setup inherently provides an ideal plane-wave excitation from the source. Across all scenarios, emphasis is placed on the influence of the unit cell design, the spatial configuration, and the distinction between near-field and far-field conditions, all of which critically shape the free-space path loss behavior introduced by the RIS.

The foundational physical mechanisms underlying RIS-assisted wireless propagation are best understood through classical electromagnetic theory. Power transfer between a transmitter and receiver in free space is governed by the directional characteristics and effective aperture areas of the antennas involved. Specifically, the power captured by a receiving antenna depends on the transmitted power, the gain of the transmitting antenna in the direction of propagation, the spatial distribution of the emitted electromagnetic field, and the effective area of the receiving antenna projected in the direction of arrival. When accounting for directionality, the power density observed at a specific location in space is shaped by the radiation pattern of the transmitting antenna. The amount of power collected by a receiver at that location is determined by the product of this power density and the receiver's directional aperture sensitivity. For practical analysis, this directional dependence is typically described using normalized radiation patterns that characterize how much energy is radiated or received in different directions.

In the case of RIS, each unit cell on the surface behaves as a passive sub-wavelength scatterer with a

defined physical area and an angular response that governs how it interacts with incident electromagnetic waves. The incident power on each unit cell depends on its orientation, distance from the source, and both the transmit antenna pattern and the cell's own angular sensitivity. Once illuminated, each unit cell reflects a portion of the incident energy toward the receiver. The strength and direction of this reflected signal are determined by the cell's complex reflection coefficient, which encapsulates a controllable amplitude and phase shift. This phase-amplitude pair can be tuned to shape the wavefront constructively or destructively at specific locations in space, thus enabling functionalities like beam steering or focusing. The contribution of each unit cell to the total received power is influenced by multiple factors: the strength of the reflected signal (which in turn depends on the power incident on the cell and the reflection coefficient), the geometric path length to the receiver, and the angular alignment between the cell and the receiving antenna. The receiver's gain in the direction of each contributing element also plays a role, as does the physical aperture of the receiver. By summarizing the individual contributions from all active RIS elements, a complete picture of the RIS-assisted channel emerges. One that captures the spatially varying interactions between transmitters, the programmable surface, and the receiver. This modeling approach allows us to study the impact of RIS configuration under different operating conditions and derive insights into optimizing RIS design for practical deployment. Considering the previously applied logic to derive the received power at the unit cell, we can describe the behavior of the reflected wave from  $U_{n,m}$  to the receive antenna, given by

$$P_{n,m}^{r} = \frac{P_{n,m}^{\text{reflected}}G}{4\pi \left(r_{n,m}^{r}\right)^{2}} F\left(\theta_{n,m}^{r}, \varphi_{n,m}^{r}\right) F^{rx}\left(\theta_{n,m}^{rx}, \varphi_{n,m}^{rx}\right) A_{r}, \tag{2.1}$$

where  $P_{n,m}^{\text{reflected}}$  is the total reflected signal power of  $U_{n,m}$ , which according to the law of energy conservation, is given by  $P_{n,m}^{\text{reflected}} = P_{n,m}^t |\Gamma_{n,m}|^2$ . On the same note,  $\Gamma_{n,m} = A_{n,m} e^{j\phi_{n,m}}$  is the reflection coefficient  $U_{n,m}$  where  $A_{n,m}$  represent the controllable amplitude bias of the unit cell and  $\phi_{n,m}$  the tunable phase shift to steer the incident electromagnetic wave.

The connection between electromagnetic field quantities and the transmitted power can be understood through the concept of power density in an electromagnetic wave. This relationship is represented by the Poynting vector, which indicates the instantaneous energy flow per unit area. It shows how the electric and magnetic fields interact to transfer energy through space. In free space, the direction of this vector aligns with the wave's propagation direction, and its magnitude reflects the instantaneous power density of the wave. For time-harmonic fields, the time-averaged power density can be directly related to the magnitude of the electric field and the intrinsic impedance of free space. This allows the electric field to be expressed as a function of the received power and the effective aperture of the receiving antenna. The expression accounts for both the spatial decay of the field with distance and the phase shift caused by wave propagation.

Within the RIS-assisted wireless communication framework, the reflected signal from each unit cell on the surface can also be described in terms of its electric field contribution. Each cell acts as a passive scatterer, and the amplitude of its reflected electric field depends on the power it receives, the effective aperture of the receiving antenna, and the impedance characteristics of the surrounding medium. This field is modulated by a phase term that includes the propagation delay along the transmitter-to-RIS and RIS-to-receiver paths, as well as the phase shift imposed by the unit cell's reflection coefficient. The reflection coefficient encompasses both a controllable amplitude scaling and a tunable phase component, which are essential for RIS-based beamforming and spatial control. The total field at the receiver is obtained by superimposing the electric field contributions from all unit cells. These contributions vary in amplitude, phase, geometric relationship to the source and receiver, and are influenced by the angular sensitivities of the antenna and the unit cells. To simplify the description, the various direction-dependent effects, such as the transmit and receive antenna patterns and the unit cell's angular response, can be combined into a single term that captures the overall angular influence on each reflection path. The collective contribution of the RIS to the received signal is thus represented as a weighted sum over all unit cells, with each term accounting for spatial position, angular sensitivity, and individual phase control. The received power can

be related back to this total field by connecting the field strength to the effective aperture of the receiving antenna. This establishes a direct link between the RIS configuration, the system's antenna characteristics, and the final received signal strength. Additionally, understanding the relationship between an individual cell's scattering gain and its physical area, often characterized by the unit cell's dimensions and operating wavelength, provides further insight into how surface geometry impacts system-level performance.

Although expressed here without explicit equations, this formulation enables a comprehensive understanding of how RIS-assisted propagation works at the electromagnetic level and supports both qualitative and quantitative analyses of RIS-enhanced wireless systems. Provided all previously made assumptions, the general pathloss formula is finally given by

$$PL = \frac{16\pi^2}{G_t G_r (d_x d_y)^2} \left| \sum_{m=1-\frac{M}{2}}^{\frac{M}{2}} \sum_{n=1-\frac{N}{2}}^{\frac{N}{2}} \frac{\sqrt{F_{n,m}^{\text{total}}}}}{r_{n,m}^t r_{n,m}^r} \Gamma_{n,m} e^{-j\frac{2\pi}{\lambda} \left(r_{n,m}^t + r_{n,m}^r\right)} \right|^{-2}.$$
(2.2)

Depending on the measurement configuration and underlying propagation assumptions, the general path loss expression can be further specialized to suit various practical scenarios. The following formulations describe the path loss in different representative cases, each derived from the general model under specific approximations. In the far-field beamforming scenario, where the RIS is illuminated under plane-wave assumptions and the observation point lies sufficiently far from the surface, the path loss simplifies to

$$PL_{\text{farfield}}^{\text{beam}} = \frac{16\pi^2 (d_1 d_2)^2}{G_t G_r (MN d_x d_y \lambda A)^2 F(\theta_t, \varphi_t) F(\theta_r, \varphi_r)}.$$
 (2.3)

In the spherical-wave near-field regime, where the wavefront curvature and spatial variation of the incident and reflected fields must be accounted for explicitly, the path loss expression becomes

$$PL_{\text{nearfield}}^{\text{beam}} = \frac{16\pi^2}{G_t G_r (d_x d_y \lambda A)^2} \left| \sum_{m=1-\frac{M}{2}}^{\frac{M}{2}} \sum_{n=1-\frac{N}{2}}^{\frac{N}{2}} \frac{\sqrt{F_{n,m}^{\text{total}}}}{r_{n,m}^r r_{n,m}^t} \right|^{-2}.$$
(2.4)

Eq. (2.3) and Eq. (2.4) have further been analyzed and simplified to also encompass broadcasting models for other modeling aspects in [20]. For compact antenna test range (CATR) setups, where a controlled quasi-plane wave is generated at the RIS but only the spherical propagation between RIS and receiver is preserved, the expression simplifies to

$$PL_{\text{CATR}}^{\text{beam}} = \frac{16\pi^2}{G_t G_r (d_x d_y)^2} \left| \sum_{m=1-\frac{M}{2}}^{\frac{M}{2}} \sum_{n=1-\frac{N}{2}}^{\frac{N}{2}} \frac{\sqrt{F(\theta_{n,m}^r, \varphi_{n,m}^r) F^{rx}(\theta_{n,m}^{rx}, \varphi_{n,m}^{rx}) F(\theta_{n,m}^t, \varphi_{n,m}^t)}}{r_{n,m}^r} \right|^{-2} . \tag{2.5}$$

While Compact Antenna Test Ranges (CATRs) are designed to simulate far-field plane-wave conditions within a limited space, they do not entirely remove the importance of path loss modeling, especially when assessing Reconfigurable Intelligent Surface (RIS) performance. In a CATR, the transmitter is replaced with a high-gain feed antenna that illuminates a large parabolic reflector, which then produces a quasi-plane wave in the quiet zone. This configuration eliminates the need to model free-space propagation from the feed to the RIS, as the incident wave is assumed to be uniform and known. However, path loss remains essential in characterizing the link between the RIS and the receiving probe antenna, typically placed within the quiet zone at a finite distance from the surface.

Because the reflected wavefront from the RIS travels along a spherical path toward the receiver, the received signal power heavily depends on the RIS's geometry, the phase profile on its surface, and the spatial

variation of field contributions across its aperture. Thus, accurately modeling this segment is vital for deriving meaningful performance metrics such as effective gain, beamforming precision, and radar cross-section enhancement. The path loss formula adapted for CATR scenarios captures these effects by considering the spherical-wave propagation from each RIS element to the receiving probe while treating the incident field as uniform.

# 2.3 COST 2100/INTERACT

A family of GSCMs spread over the models established during the previous programs delegated by the European Cooperation in Science and Technology (COST). While the COST 259 was the first model of this kind that allowed the existence of antenna arrays on the base station (BS) side, COST 273 upgraded existing features by involving antenna arrays to be present at the mobile station (MS) side. In order to overcome a lack of multi-user configuration of COST 273, the COST 2100 provided multi-user setup in both, single-cell and multi-cell environments also taking cooperative aspects into account.

# 2.3.1 Single-link implementation

The original COST 2100 could be called single-link COST 2100 and refers to a double-directional model capable of reproducing properties of MIMO channels over space and frequency. It supports concurrent modeling of a radio link between a single pair consisting only of one BS and one or more MSs in a static propagation environment.

For simplicity, the model [21] considers electromagnetic (EM) wave interactions exclusively with a special case of scatterers. These scatterers act like reflectors producing specular reflections. The specular reflection presents an EM wave reflected by respecting the law-of-optics which does not exhibit any additional propagation attenuation besides of free-space path-loss (FSPL), while offering the pure conservation of the previously radiated power. A scatterer is modeled as an imaginary object being an infinitely sized and perfectly smooth for mid-band frequency by producing a single propagation path, obviously adding a non-realistic aspect to the model [22]. All formed reflections are entitled as multi-path components (MPCs). By observing the characteristics of individual MPCs, findings indicate similarities across the MPCs interacting with the specific set of scatterers. Thanks to the common physical properties like time-delays and directions, MPCs are being grouped into clusters allowing for the MPCs parameterization and implicitly reducing the complexity of their description like shown at the Fig. 2.7.

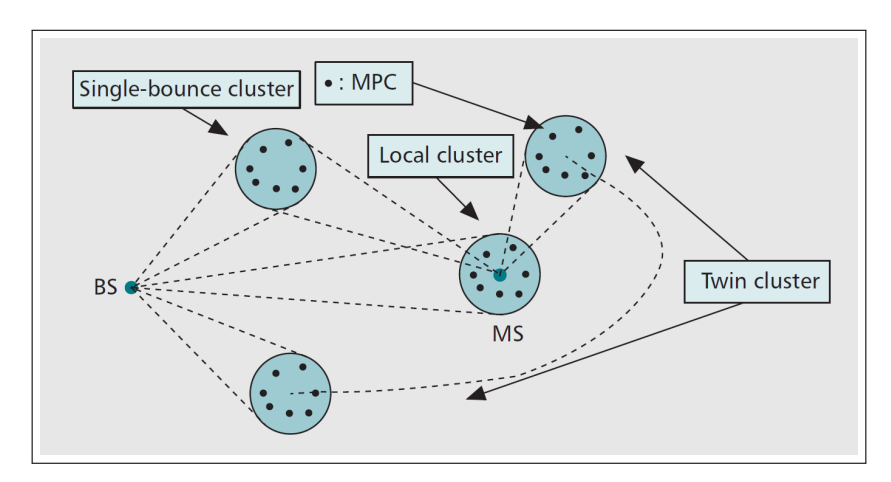


Figure 2.7: Planar description of the single-link COST 2100 channel model. [21]

Depending on the relative distance from a cluster to the BS or MSs, there exists two types of clusters in

the model, named local and far clusters. The previous one confines the interactions of EM waves to single bounce reflections, while the latter one tolerates multi-bounces, as well. When it comes to the local clusters, as a consequence of a single-bounce effect, the positions of these clusters are not only constrained by the proximity to the BS or MSs, but also with the orientation to all other clusters. In other words, for any local cluster, the model aims to maintain all other clusters non-visible to prevent multi-bounces. Therefore, there exists a position dependence of inter-local clusters and local-far clusters.

Exclusively for the far clusters, the model involves a concept of a visibility region (VR) that is a circular region of a fixed size determining the visibility of only one far cluster from BS and MS perspective. Whether the far clusters provide single or multi-bouncing, the VR are randomly distributed in the simulation area with a possibility for more VRs to overlap. According to spatial representation of all kinds of clusters given at Fig. 2.8, it is noticeable that an ellipsoid corresponding to a far field cluster capable of multi-bouncing at Fig. 2.8 c) requires geometrical projections onto two circles. These circles hold a joint name - twin clusters. The explanation behind the projections can be found in the need to capture the perspective of a far multi-bouncing cluster from both, a BS and a MS.

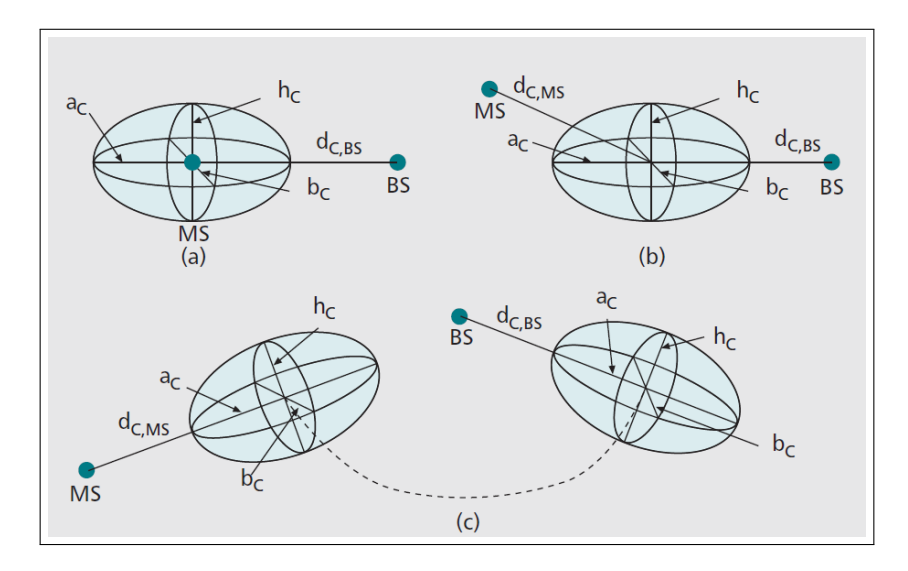


Figure 2.8: Spatial description of a) local; b) far single-bounce; c) twin clusters involved into the single-link COST 2100 channel model:  $a_c$ ,  $b_c$ , and  $b_c$  represent the length, width, and height of the cluster;  $d_{C, MS}$  and  $d_{C,BS}$  are the distances from the cluster to the MS and BS, respectively. [21]

# 2.3.2 Multi-link extension

The term 'multi-link' opens the door to the concurrent channel's characterization between multiple BS and multiple spatially distributed MSs. In this way, the limitation in the 'single-link' model related to the incorporating simultaneous channel characterization of multiple BSs is now exceeded. Considering that clusters may be visible in different links, it actually served as a proposal for the extension and implementation of the 'multi-link' model.

This enhanced model [21] includes reproducing conditions of MIMO channels also over time. Hence, a feature of modeling time-selective channels got incorporated by omitting any restriction to the velocity of a moving MSs.

Motivated to include diffuse scattering effects present in practice, the model deploys so-called dense multipath components (DMCs). It refers to the superposition of a large number of specular reflections, but with modified properties. The DMC characterization is achieved at a cluster level.

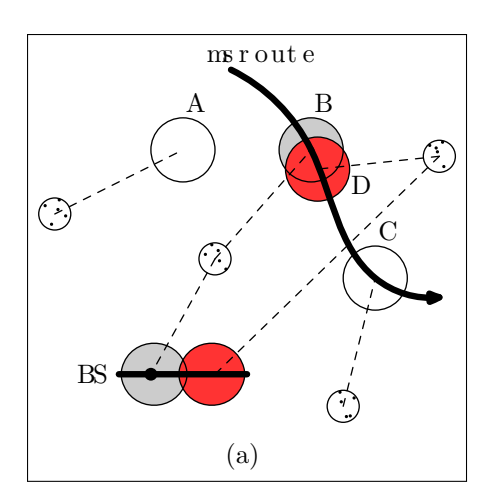
Polarization aspects are also described on a cluster level, while an MPC contains linear polarization com-

ponents: vertical-to-vertical (VV), horizontal-to-horizontal (HH), vertical-to-horizontal (VH), horizontal-to-vertical (HV).

#### 2.3.3 Massive MIMO extensions

The Massive MIMO theoretical papers considered simulated and especially non-physical/analytical channel models to demonstrate a significant improvement in terms of throughput and coverage under a specific ratio of a number of BS and single-antenna MSs. It triggered the investigation of the spatial consistency of so-called physically large arrays (PLAs) in the existing channel models. In that light, the need for the extension of multi-link COST 2100 brang attraction. The so-called MaMi extensions [23] proposes two novel developments to answer following challenges: BS-side non-stationarities of the clusters and MS-side birth-death processes of individual MPCs.

BS-side non-stationarities are addressed by the extended BS-VRs concept. The novelty here comparing to the method implemented in multi-link model refers to the conclusions coming from measured MaMi channels, afterwards being properly modeled. Appearance and disappearance of clusters along the axis of a PLA at BS that causes BS-side non-stationarities received an adequate formulation as illustrated at Fig. 2.9 a). Another challenge, MS-side birth-death processes, becomes covered by the utilization of MPC-VRs and MPC gain function. Although the MPC-VRs strategy also was noticable in the model predecessor for twin-clusters purposes, this time, together with MPC gain function, it tends to describe birth-death processes of individual MPCs as shown at Fig. 2.9 b).



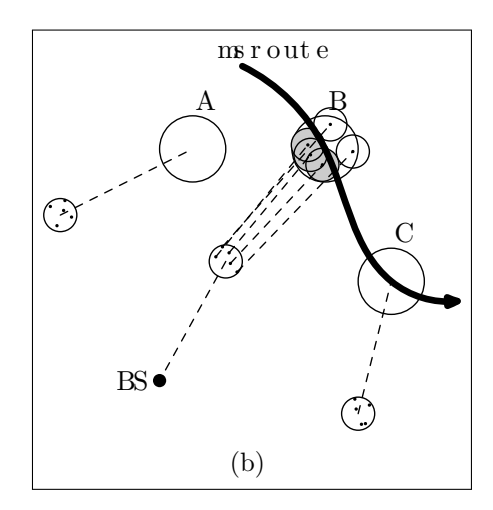


Figure 2.9: a) Different parts of PLA can observe different sets of clusters (VR B, or VR D, or VRs B and D), as determined by BS-VRs. (b) The relative channel gain of individual MPCs is controlled by MPC-VRs, one for each MPC. [23]

# 2.3.4 Extension for D-MIMO

D-MIMO systems being spatially separated impacts on reducing large-scale fading, as one of statistical measures, while their modeling requires taking spatial and temporal non-stationarities into consideration, [24]. Therefore, it is promising to incorporate D-MIMO perspective into a measurement based model based on above described COST 2100 advantages. One such model is "Spatially consistent distributed MIMO channel model for industrial environments", [25]. Although the measurements have been done in the sub-6GHz bands, the model has a potential for adjustments to upper mid-band frequencies. The details of an approach for classifying obstruction in terms of available LiDAR data and approximated the first Fresnel zone are available in [24]. It is worth of noting that this model confirmed the presence of a significant

channel hardening able to combat the small-scale fading effects. The model improvements could be seen in addressing effects of moving machinery or robots to the channel response.

### 2.3.5 Other extensions

When it comes to the ultra massive MIMO systems, the main requirements spread over spatial non-stationarities and utilization of spherical wavefronts. Therefore, the existing MaMi COST 2100 model already possess the methods to deal with these challenges. However, the paper [26] discusses actual limitations in the MaMi extension. MS-VR is modeled as a circle without a support to simulate a scenario of MSs positioned on different floors. Also, the BS-VRs are valid only for uniform linear arrays, while in practice, the most common array configuration is a planar one with uniformly separated elements.

# 2.4 WiFi sense and 802.11 distributed MIMO

Significant activities of IEEE 802.11 development have been conducted through Task Groups (TGs). In parallel with the advancements in distributed MIMO for enhancing spatial diversity and throughput in WLANs, the TGbf or popularly IEEE 802.11bf amendment introduces a complementary capability: Wi-Fi sensing. This technique leverages the sensitivity of Wi-Fi signals to environmental changes, enabling applications such as proximity detection, gesture recognition, and health monitoring. The 802.11bf Task Group has defined essential PHY and MAC layer protocols to support sensing across sub-7 GHz and 60 GHz bands, allowing Wi-Fi devices to perform over-the-air measurements and report sensing data in a standardized manner. These developments not only expand the functional scope of Wi-Fi networks but also align with the broader vision of integrating communication and sensing within the same infrastructure [27]. Moreover, Wi-Fi sensing benefits from the same multi-device coordination principles found in distributed MIMO. Field measurements have shown that sensing accuracy improves with increased transmit and receive diversity, which can be achieved through cooperation among multiple Wi-Fi devices. The standardized mechanisms introduced in 802.11bf, such as negotiated transmission parameters and interoperable sensing protocols, enable reliable and scalable sensing deployments, paving the way for joint communication-sensing systems within WLAN environments [27].

Following the report objectives, an introduction of MIMO channel models comes by the efforts of TGn (High Throughput Task Group). In terms of intended frequency range, the model is suited for utilization with the lower mid-band, precisely, 2.4 GHz and 5 GHz. By the appearance of TGac, TGax, TGah, and TGbf, sorted in dating order, the validated frequency range remains unchanged. Besides these, TGad and TGay are convenient examples of validated channel models for usage on 60GHz. However, this frequency range is out of the report scope.

TGn, [28] aims to characterize angular and power properties of indoor wideband MIMO channels with the system bandwidth limited to 40 MHz. This has been done by applying a cluster modeling approach. The cluster modeling approach has roots in Saleh-Valenzuela model [29], while certain adaptations of this model, e.g. for ultrawideband purposes, [30] are also available. Being originally introduced for indoor wideband systems, it models the arrivals of both: MPCs in clusters and these clusters by Poisson processes. The TGn model provides the MIMO channel impulse response in the form of a matrix. The correlations amongst the entries in the MIMO matrix are taken into account by Kronecker model [31]. As one of methods for (de)coupling transmitting and receiving side of MIMO link, the Kronecker model decouples transmitting and receiving antennas that is a desirable in the cases of separable AoA-AoD spectra, as validated in [32]. According to [33], TGac (Very High Throughput Task Group) extends functionality of TGn by reducing PDP minimum tap spacing, while now being employed for system bandwidth at most of 1.28 GHz. For the mentioned system bandwidth, PDP minimum tap spacing equals 0.3125 ns. It is worth noting that

occuring a tap interpolation results in independent channel tap realizations. As a consequence, this model presents fundamentally different channel model compared to TGn. By maintaining the employed antenna correlations model in TGn, TGac use cases shift towards higher order MIMO than  $4 \times 4$ . In addition, multiuser channels are now covered by modification of AoDs and AoAs. At the end, dual-polarized antennas are incorporated into the model.

TGax (High Efficiency Wireless LAN Task Group) [34] has a primary goal to improve the average throughput per station, while it targets both indoor and outdoor scenarios. For the previous one, it combines its predecessors, TGn and TGac. In the case of the latter one, the model adopts ITU-R M.2135-1 channel model [35] by enhancing system bandwidth to support 160 MHz. Also, TGax brings Doppler modes for pedestrian mobility and fast moving objects.

TGah (Extended Range (< 1 GHz) Task Group) [36] co-opts TGn and TGac model to combine them for indoor purposes, as it is a case for TGax. Similarly, but with a minor dissimilarity, TGax consists of 3GPP TR 25.996 [37] and TGn model to cope with outdoor applications.

To the best of the authors' knowledge, there is no currently available channel model from TGs that offers distributed MIMO advantages. Conceptually, it means that Access Points (APs) collaborate in order to achieve higher performances compared to the systems with co-located APs. The critical request for enhancing performances in this way is a synchronization amongst the APs. This also may represent upcoming research direction of TGs by taking into account the progress made with the cell-free channel models, e.g. Cell-free massive MIMO for Urban Non-stationary Environment with Correlations (CUNEC) model, [38].

# Chapter 3

# Summary and conclusions

The transition toward FR3 is not merely a shift in operating frequency but a key step toward redefining the architecture and capacities of next-generation wireless systems. Situated between the well-established FR1 and the high-capacity yet range-limited FR2, FR3 offers a unique opportunity to integrate the advantages of both: wide-area coverage with significantly enhanced capacity. This spectrum window, coupled with advanced physical-layer technologies, is well-positioned to support ultra-massive MIMO, distributed antenna systems, and integrated sensing and communication functions while maintaining infrastructure efficiency through minimal alterations to existing site grids.

To fully exploit FR3's potential, accurate and adaptable channel models must be developed that capture its specific propagation dynamics, including frequency-dependent fading characteristics, spatial consistency, and environment-specific multipath effects. Refining established frameworks such as 3GPP TR 38.901, COST 2100/INTERACT, and Wi-Fi sensing models will be instrumental in ensuring reliable simulation and performance prediction.

This entails expanding current models to accommodate diverse deployment scales, heterogeneous environments, and novel enablers such as reconfigurable intelligent surfaces, joint communication and radar sensing, and AI-driven channel estimation. The research community's ability to characterize FR3 propagation with high fidelity will directly influence the efficiency of spectrum allocation, the robustness of link adaptation strategies, and the scalability of network designs.

Accurate models will enhance the optimization of beamforming, resource scheduling, and interference management in dense urban, suburban, and indoor environments, where FR3 is expected to play a key role. Looking ahead, FR3 is set to become a fundamental component of the 6G ecosystem, supporting a wide range of applications, including immersive extended reality, ultra-reliable low-latency communications, advanced vehicular connectivity, and pervasive environmental sensing. The integration of communication and sensing within this frequency band could open up entirely new service paradigms, transforming networks from mere data transport platforms into intelligent perception systems.

In conclusion, the transition to FR3 presents both a technical challenge and a strategic opportunity. By engaging in thorough channel modeling, encouraging cross-domain innovation, and fostering collaboration among academia, industry, and standardization bodies, FR3 can effectively bridge the performance gap between coverage and capacity. This will help fulfill the promise of 6G to connect, sense, and serve an increasingly intelligent and interconnected world.

# References

- [1] E. Björnson, F. Kara, N. Kolomvakis, A. Kosasih, P. Ramezani, and M. B. Salman, "Enabling 6G Performance in the Upper Mid-Band by Transitioning From Massive to Gigantic MIMO," *IEEE Open Journal of the Communications Society*, vol. 6, pp. 5450–5463, 2025.
- [2] H. Holma, H. Viswanathan, and P. Mogensen, "Extreme massive MIMO for macro cell capacity boost in 5G-Advanced and 6G," Nokia, Espoo, Finland, Technical Report CID210786, 2021.
- [3] K. T. Truong and R. W. Heath, "The viability of distributed antennas for massive MIMO systems," in 2013 Asilomar Conference on Signals, Systems and Computers, 2013, pp. 1318–1323.
- [4] C. Masouros, M. Sellathurai, and T. Ratnarajah, "Large-Scale MIMO Transmitters in Fixed Physical Spaces: The Effect of Transmit Correlation and Mutual Coupling," *IEEE Transactions on Communi*cations, vol. 61, no. 7, pp. 2794–2804, 2013.
- [5] L. Sanguinetti, E. Björnson, and J. Hoydis, "Toward Massive MIMO 2.0: Understanding Spatial Correlation, Interference Suppression, and Pilot Contamination," *IEEE Transactions on Communications*, vol. 68, no. 1, pp. 232–257, 2020.
- [6] J. Hoydis, S. ten Brink, and M. Debbah, "Massive MIMO in the UL/DL of Cellular Networks: How Many Antennas Do We Need?" *IEEE Journal on Selected Areas in Communications*, vol. 31, no. 2, pp. 160–171, 2013.
- [7] E. Björnson, J. Hoydis, and L. Sanguinetti, "Massive MIMO Networks: Spectral, Energy, and Hardware Efficiency," Foundations and Trends in Signal Processing, vol. 11, no. 3–4, pp. 154–655, 2017.
- [8] X. Gao, O. Edfors, F. Rusek, and F. Tufvesson, "Linear Pre-Coding Performance in Measured Very-Large MIMO Channels," in *Proc. IEEE Vehicular Technology Conference*, 2011, pp. 1–5.
- [9] H. Q. Ngo and E. G. Larsson, "No Downlink Pilots Are Needed in TDD Massive MIMO," *IEEE Transactions on Wireless Communications*, vol. 16, no. 5, pp. 2921–2935, 2017.
- [10] Z. Chen and E. Björnson, "Channel Hardening and Favorable Propagation in Cell-Free Massive MIMO With Stochastic Geometry," *IEEE Transactions on Communications*, vol. 66, no. 11, pp. 5205–5219, 2018.
- [11] 3GPP TSG RAN WG1, "Views on rel-19 ISAC channel modelling," 3GPP TSG RAN WG1, Technical Contribution R1-2407211, Aug. 2024, 3GPP TSG RAN WG1 #118.
- [12] M. I. Skolnik, Ed., Radar Handbook, 3rd ed. McGraw-Hill, 2008.
- [13] W. Yang, Y. Chen, Y. Zhang, Z. Yu, and M. Zhang, "ISAC Channel Measurements and Modeling Methodology," in 2023 IEEE Globecom Workshops (GC Wkshps), 2023, pp. 1177–1182.

- [14] 3rd Generation Partnership Project (3GPP), "Study on channel model for frequencies from 0.5 to 100 GHz," European Telecommunications Standards Institute (ETSI), Technical Report ETSI TR 138 901 V18.0.0, May 2024. [Online]. Available: https://www.etsi.org/deliver/etsi\_tr/138900\_138999/138901/18.00.00\_60/tr\_138901v180000p.pdf
- [15] 3rd Generation Partnership Project (3GPP), "3GPP TR 36.873 V12.2.0: Study on 3D Channel Model for LTE," 3GPP, Technical Report 36.873, June 2015, release 12. [Online]. Available: https://www.3gpp.org/ftp/Specs/archive/36\_series/36.873/
- [16] X. You, C.-X. Wang, J. Huang, X. Gao, Z. Zhang, M. Wang, Y. Huang, C. Zhang, Y. Jiang, J. Wang et al., "Towards 6G wireless communication networks: Vision, enabling technologies, and new paradigm shifts," Science China information sciences, vol. 64, no. 1, p. 110301, 2021.
- [17] T. Jiang, J. Zhang, P. Tang, L. Tian, Y. Zheng, J. Dou, H. Asplund, L. Raschkowski, R. D'Errico, and T. Jämsä, "3GPP Standardized 5G Channel Model for HoT Scenarios: A Survey," *IEEE Internet of Things Journal*, vol. 8, no. 11, pp. 8799–8815, 2021.
- [18] 3rd Generation Partnership Project (3GPP), "3GPP TS 22.137 V19.3.0: Service Requirements for Integrated Sensing and Communication (ISAC)," 3rd Generation Partnership Project (3GPP), Technical Specification 22.137, March 2024, release 19. [Online]. Available: https://www.3gpp.org/ftp/Specs/archive/22\_series/22.137/
- [19] —, "3GPP TR 22.837 V19.3.0: Feasibility Study on Integrated Sensing and Communication (ISAC)," 3rd Generation Partnership Project (3GPP), Technical Report 22.837, March 2024, release 19. [Online]. Available: https://www.3gpp.org/ftp/Specs/archive/22\_series/22.837/
- [20] W. Tang, M. Z. Chen, X. Chen, J. Y. Dai, Y. Han, M. Di Renzo, and T. J. Cui, "Wireless communications with reconfigurable intelligent surface: Path loss modeling and experimental measurement," *IEEE Transactions on Wireless Communications*, vol. 20, no. 1, pp. 421–439, 2020.
- [21] L. Liu, C. Oestges, J. Poutanen, K. Haneda, P. Vainikainen, F. Quitin, F. Tufvesson, and P. Doncker, "The COST 2100 MIMO channel model," *IEEE Wirel. Commun.*, vol. 19, no. 6, pp. 92–99, Dec. 2012.
- [22] E. Björnson and Ö. T. Demir, Introduction to Multiple Antenna Communications and Reconfigurable Surfaces. Now Publishers, 2024.
- [23] J. Flordelis, X. Li, O. Edfors, and F. Tufvesson, "Massive MIMO extensions to the COST 2100 channel model: Modeling and validation," *IEEE Trans. Wirel. Commun.*, vol. 19, no. 1, pp. 380–394, Jan. 2020.
- [24] C. Nelson, S. Willhammar, and F. Tufvesson, "A Measurement-Based Spatially Consistent Channel Model for Distributed MIMO in Industrial Environments," 2025. [Online]. Available: https://arxiv.org/abs/2412.12646
- [25] —, "A Measurement-Based Spatially Consistent Channel Model for Distributed MIMO in Industrial Environments," 2025. [Online]. Available: https://arxiv.org/abs/2412.12646
- [26] L. Fan, Z. Zhong, C. Wang, Q. Qin, W. Han, and T. Wang, "Extensions to COST 2100 channel model for extremely large-scale MIMO," in 2022 IEEE 95th Vehicular Technology Conference: (VTC2022-Spring). IEEE, Jun. 2022.
- [27] C. Chen, H. Song, Q. Li, F. Meneghello, F. Restuccia, and C. Cordeiro, "Wi-Fi Sensing Based on IEEE 802.11bf," *IEEE Communications Magazine*, vol. 61, no. 1, pp. 121–127, 2023.

- [28] V. Erceg, L. Schumacher, and P. Kyritsi, "TGn Channel Models, document," IEEE, Technical Report IEEE 802.11-03/0940r4, May 2004.
- [29] A. A. M. Saleh and R. Valenzuela, "A statistical model for indoor multipath propagation," *IEEE J. Sel. Areas Commun.*, vol. 5, no. 2, pp. 128–137, Feb. 1987.
- [30] A. F. Molisch, J. R. Foerster, and M. Pendergrass, "Channel models for ultrawideband personal area networks," *IEEE Wirel. Commun.*, vol. 10, no. 6, pp. 14–21, Dec. 2003.
- [31] J. P. Kermoal, L. Schumacher, K. I. Pedersen, P. E. Mogensen, and F. Frederiksen, "A stochastic MIMO radio channel model with experimental validation," *IEEE J. Sel. Areas Commun.*, vol. 20, no. 6, pp. 1211–1226, Aug. 2002.
- [32] C. Oestges, "Validity of the Kronecker model for MIMO correlated channels," in 2006 IEEE 63rd Vehicular Technology Conference. IEEE, 2006.
- [33] G. Breit, H. Sampath, S. Vermani, and et al., "TGac Channel Model Addendum," IEEE, Technical Report IEEE 802.11-09/0308r12, Mar. 2010.
- [34] L. Jianhan, P. Ron, and et al., "TGax Channel Model," IEEE, Technical Report IEEE 802.11-14/0882r4, Sep. 2014.
- [35] "Guidelines for Evaluation of Radio Interface Technologies for IMT-Advanced," ITU, Technical Report ITU-R Rep. M.2135-1, 2009.
- [36] R. Porat, S. K. Yong, and K. Doppler, "TGah Channel Model," IEEE, Technical Report IEEE 802.11-11/0968r4, Mar. 2015.
- [37] "Spatial channel model for Multiple Input Multiple Output (MIMO) simulations," 3GPP, Technical Report 3GPP TR 25.996, 2017.
- [38] T. Choi, I. Kanno, M. Ito, W.-Y. Chen, and A. F. Molisch, "A realistic path loss model for cell-free massive MIMO in urban environments," in *GLOBECOM 2022 2022 IEEE Global Communications Conference*. IEEE, Dec. 2022.
- [39] J. Zhang, H. Miao, P. Tang, L. Tian, and G. Liu, "New Mid-Band for 6G: Several Considerations from the Channel Propagation Characteristics Perspective," *IEEE Communications Magazine*, vol. 63, no. 1, pp. 175–180, 2025.
- [40] —, "New Mid-Band for 6G: Several Considerations from the Channel Propagation Characteristics Perspective," *IEEE Communications Magazine*, vol. 63, no. 1, pp. 175–180, 2025.